Freshly Formed Dust in the Cassiopeia A Supernova Remnant as Revealed by the *Spitzer* Space Telescope

J. Rho[1], T. Kozasa[2], W. T. Reach[1], J. D. Smith[3], L. Rudnick[4], T. DeLaney[5], J. A. Ennis[4], H. Gomez[6], A. Tappe[1,7]

ABSTRACT

We performed *Spitzer* Infrared Spectrograph mapping observations covering nearly the entire extent of the Cassiopeia A supernova remnant (SNR), producing mid-infrared (5.5-35 μm) spectra every $5''$-$10''$. Gas lines of Ar, Ne, O, Si, S and Fe, and dust continua were strong for most positions. We identify three distinct ejecta dust populations based on their continuum shapes. The dominant dust continuum shape exhibits a strong peak at 21 μm. A line-free map of 21 μm-peak dust made from the 19-23 μm range closely resembles the [Ar II], [O IV], and [Ne II] ejecta-line maps implying that dust is freshly formed in the ejecta. Spectral fitting implies the presence of SiO_2, Mg protosilicates, and FeO grains in these regions. The second dust type exhibits a rising continuum up to 21 μm and then flattens thereafter. This "weak 21 μm" dust is likely composed of Al_2O_3 and C grains. The third dust continuum shape is featureless with a gently rising spectrum and is likely composed of $MgSiO_3$ and either Al_2O_3 or Fe grains. Using the least massive composition for each of the three dust classes yields a total mass of 0.020 $M_\odot$. Using the most-massive composition yields a total mass of 0.054 $M_\odot$. The primary uncertainty in the total dust mass stems from the selection of the dust composition necessary for fitting the featureless dust as well as 70 μm flux. The freshly formed dust mass derived from Cas A is sufficient from SNe to explain the lower limit on the dust masses in high redshift galaxies.

[1]*Spitzer* Science Center, California Institute of Technology, Pasadena, CA 91125; rho, reach@ipac.caltech.edu

[2]Department of Cosmosciences, Graduate School of Science, Hokkaido University, Sapporo 060-0810, Japan

[3]Steward Observatory, 933 N. Cherry Ave., Tucson, AZ 85712

[4]Department of Astronomy, University of Minnesota, 116 Church St. SE, Minneapolis, MN 55455

[5]MIT Kavli Institute, 77 Massachusetts Ave., Room NE80-6079, Cambridge, MA 02139

[6]School of Physics and Astronomy, University of Wales, Cardiff, Wales, UK

[7]Harvard-Smithsonian Center for Astrophysics, 60 Garden Street, Cambridge, MA 02138

Subject headings: supernovae:general- dust:ISM - supernova remnants:Cas A

1. Introduction

The recent discovery of huge quantities of dust ($10^8 - 10^9\,\mathrm{M_\odot}$) in very high–redshifted galaxies and quasars (Isaak et al. 2002; Bertoldi et al. 2003) suggests that dust was produced efficiently in the first generation of supernovae (SNe). Theoretical studies (Kozasa et al. 1991; Todini & Ferrara 2001, hereafter TF; Nozawa etal. 2003, N03) predicted the formation of a significant quantity of dust ($\sim 0.1 - 1.0\ M_\odot$) in the ejecta of Type II SNe, and the predicted dust mass is believed to be sufficient to account for the quantity of dust observed at high redshifts (Maiolino et al. 2006; Meikle et al. 2007). Recently, a model of dust evolution in high–redshift galaxies (Dwek et al. 2007) indicates that at least 1 $M_\odot$ of dust per SN is necessary for reproducing the observed dust mass in one hyperluminous quasar at $z = 6.4$. Observationally, the presence of freshly formed dust has been confirmed in a few core-collapsed SNe, such as SN1987A, which clearly have showed several signs of dust formation in the ejecta (see McCray 1993 for details). The highest dust mass obtained so far for SN 1987A is $7.5 \times 10^{-4}\ M_\odot$ (Ercolano et al. 2007). Recent *Spitzer* and *HST* observations (Sugerman et al. 2006) showed that up to 0.02 $M_\odot$ of dust formed in the ejecta of SN2003gd with the progenitor mass of 6–12 $M_\odot$, and the authors concluded that SNe are major dust factories. However, from the detailed analysis of the late–time mid–infrared observations, Meikle et al. (2007) found that the mass of freshly formed dust in the same SN is only $4 \times 10^{-5}M_\odot$, and failed to confirm the presence 0.02 $M_\odot$ dust in the ejecta. The aforementioned results show that the derived dust mass is model-dependent, and that the amount of dust that really condenses in the ejecta of core-collapsed SNe is unknown.

Cassiopeia A (Cas A) is the only Galactic supernova remnant (SNR) that exhibits clear evidence of dust formed in ejecta (Lagage et al. 1996; Arendt et al. 1999, hereafter ADM). The amount of dust that forms in the ejecta of young SNR is still controversial. Previous observations inferred only $< 3 \times 10^{-3}\,\mathrm{M_\odot}$ of dust at temperatures between 90 and 350 K (ADM; Douvion et al. 2001, hereafter D01) ; this estimate is 2 to 3 orders of magnitude too little to explain the dust observed in the early Universe. Recent submillimeter observations of Cas A and Kepler with SCUBA (Dunne et al. 2003; Morgan et al. 2003) revealed the presence of large amounts of cold dust ($\sim 0.3 - 2\,\mathrm{M_\odot}$ at 15–20 K) missed by previous IRAS/ISO observations. On the other hand, highly elongated conductive needles with mass of only 10^{-4} to $10^{-3}\ M_\odot$ could also explain a high sub-mm flux of Cas A, when including grain destruction by sputtering (Dwek 2004), though the physicality of such needles is doubtful (Gomez et al. 2005). While Krause et al. (2005) showed that much of the 160μm emission

observed with Multiband Imaging Photometer for *Spitzer* (MIPS) is foreground material, suggesting there is no cold dust in Cas A, Wilson & Batrla (2005) used CO emission towards the remnant to show that up to about a solar mass of dust could still be associated with the ejecta, not with the foreground material. These controversial scenarios of dust mass highlight the importance of correctly identifying the features and masses of dust freshly formed in Cas A. The Galactic young SNR Cas A allows us to study in detail the distribution and the compositions of the dust relative to the ejecta and forward shock with infrared Spectrograph onboard the *Spitzer Space Telescope*.

Cas A is one of the youngest Galactic SNRs with an age of 335 yr attributed to a SN explosion in AD 1671. The progenitor of Cas A is believed to be a Wolf-Rayet star with high nitrogen abundance (Fesen 2001) and to have a mass of 15-25 $M_\odot$ (Kifonidis et al. 2000; Young et al. 2006) or 29-30 $M_\odot$ (Pérez-Rendón et al. 2002). The predicted dust mass formed in SNe depends on the progenitor mass; for a progenitor mass of 15 to 30 $M_\odot$, the predicted dust mass is from 0.3 to 1.1 $M_\odot$ (NO3) and from 0.08 to 1.0 $M_\odot$ (TF), respectively. In this paper, we present *Spitzer* Infrared Spectrograph (IRS) mapping observations of Cas A, and identify three distinct classes of dust associated with the ejecta and discuss dust formation and composition with an estimate of the total mass of freshly formed dust.

2. The IRS Spectra and Dust Maps

We performed *Spitzer* IRS mapping observations covering nearly the entire extent of Cas A on 2005 January 13 with a total exposure time of 11.3 hr. The Short Low (SL: 5-15 μm) and Long Low (LL: 15-40 μm) IRS mapping involved $\sim$16×360 and 4 × 91 pointings, producing spectra every 5$''$ and 10$''$, respectively. The spectra were processed with the S12 version of the IRS pipeline using the CUBISM package (Kennicutt et al. 2003; Smith et al. 2007), whereby backgrounds were subtracted and an extended emission correction was applied. The spectral resolving power of the IRS SL and LL modules ranges from 62 to 124.

The IRS spectra of Cas A show bright ejecta emission lines from Ar, Ne, S, Si, O, and Fe and various continuum shapes as indicated by the representative spectra in Figure 1. The most common continuum shape exhibits a large bump peaking at 21 μm as shown by spectrum "a" in Figure 1. This "21 μm-peak" dust is often accompanied by the silicate emission feature at 9.8 μm which corresponds to the stretching mode. A second class of continuum shapes exhibits a rather sharp rise up to 21 μm and then stays flat thereafter. This "weak-21 μm dust" is often associated with relatively strong Ne lines (in comparison with Ar lines) and is indicated by spectrum "b" in Figure 1. The third type of dust continuum is characterized by a smooth and featureless, gently rising spectrum with strong [O IV]+[Fe II]

and [Si II] emission lines as shown by spectra "c" and "d" in Figure 1. The spectrum "d" shows double line structures that may be due to doppler-resolved lines of [O IV] at 26 μm and [Si II] at 35 μm. Note that the "featureless" dust (spectrum "d" in Fig. 1) is a class of dust, separate from the interstellar/circumstellar dust (spectrum "e" in Fig. 1) heated by the forward shock. The interstellar/circumstellar dust spectrum in Cas A has no associated gas line emission. The "broad" continuum (see Figure 7b of Ennis et al. 2006) is a combination of the spectra "c" and "e". The spectrum "c" has contamination from the shock heated dust in projection, and for simplicity it is excluded in estimating the masses of the freshly formed dust (see §5). The "featureless" dust lacks the gentle peak around 26 μm and also lacks the interstellar silicate-emission feature between 9 μm and 11 μm observed in the spectra from the forward shock region. Most importantly, the "featureless" dust accompanies relatively strong Si and S ejecta lines and mostly from the interior of the remnant (blue region in Fig. 2f).

We generated a map of the 21 μm-peak dust by summing the emission over 19-23 μm after subtracting a baseline between 18-19 μm and 23-24 μm. The line-free dust map (Fig. 2a) resembles the [Ar II] and [O IV]+[Fe II] ejecta-line maps, as shown in Figures 2b and 2c, and we also find that the [Ne II] map is very similar to the [Ar II] map. The [Ar II] map shows a remarkable similarity to the 21 μm-peak dust map (Fig. 2a and 2b), thereby confirming this dust is freshly formed in the ejecta. Maps of [Si II] (Fig. 2d) and [O IV]+[Fe II] (Fig. 2c) shows significant emission at the center revealing ejecta that have not yet been overrun by the reverse shock (unshocked ejecta). There is also [Si II] and [O IV]+[Fe II] emission at the bright ring indicating that some of the Si and O+Fe ejecta have recently encountered the reverse shock. While the bright O+Fe emission outlines the same bright ring structure as the [Ar II] and 21 μm-peak dust maps, the bright part of the Si shell shows a different morphology from the other ejecta maps.

We can characterize the spectra of our three dust classes by using the flux ratios between 17 μm and 21 μm and between 21 μm and 24 μm. Although the spectra in Cas A show continuous changes in continuum shape from strong 21 μm peak to weak 21 μm peak and to featureless, we can locate regions where each of the three classes dominates. Figure 2f shows the spatial distribution of our three dust classes where red, green, and blue indicate 21 μm-peak dust, weak-21 μm dust, and featureless dust, respectively. The flux ratios used to identify the three dust classes are as follows where I_λ is the flux density in the extracted spectrum at wavelength λ (μm):

1) 21 μm-peak dust: we use the ratio $I_{21}/I_{24} > 1+\sigma_{21/24}$, where $\sigma_{21/24}$ is the dispersion in I_{21}/I_{24} over the remnant, which is equivalent to $I_{21}/I_{17} \geq 3.4$. The regions with 21 μm-peak dust coincide with the brightest ejecta.

2) Weak-21 μm dust: we use the ratio $1 - \sigma_{21/24} < I_{21}/I_{24} < 1 + \sigma_{21/24}$, which is equivalent to $2.3 < I_{21}/I_{17} < 3.4$. The regions showing the weak-21 μm continuum shape mostly coincide with faint ejecta emission, but not always.

3) Featureless dust map: we use the ratio $I_{21}/I_{24} < 1 - \sigma_{21/24}$, which is equivalent to $I_{21}/I_{17} < 2.3$. This ratio also picks out circumstellar dust heated by the forward shock, so we used several methods to exclude and mitigate contamination from circumstellar dust emission. First, using X-ray and radio maps, we excluded the forward shock regions at the edge of the radio plateau (Gotthelf et al. 2001). Second, there are highly structured "continuum-dominated" X-ray filaments across the face of the remnant which are similar to the exterior forward shock filaments and may be projected forward shock emission (DeLaney 2004). For our analysis, we excluded regions where there were infrared counterparts to the projected forward shock filaments. Third, for simplicity we excluded regions with gently rising spectra identified by curve "c" (the spectra which continues to rise to longer wavelengths) in Figure 1. This type of spectrum is mainly found on the eastern side of Cas A where there is an Hα region, the northeast jet, and other exterior optical ejecta (Fesen 2001) making it difficult to determine if the continuum emission is due to ejecta dust or circumstellar dust. However, note that some portion of the continuum in the spectra, "c", is freshly formed dust. We finally excluded regions where there was a noticeable correlation to optical quasi-stationary flocculi (van den Bergh 1971) which are dense circumstellar knots from the progenitor wind.

The featureless dust emission appears primarily across the center of the remnant, as shown in Figure 2d (blue). The featureless dust is accompanied by relatively strong [Si II] and [S III] and [O IV+Fe II] lines, as shown by the spectrum "d" of Figure 1. The [O IV]+[Fe II] line map (Fig. 2c) shows significant emission at the center as well as at the bright ring of the reverse shocked material. The [Si II] line map shows different morphology than other line maps and the 21 μm-peak dust map; depicting center-filled emission with a partial shell, as shown in Figure 2. This poses the following important question: why is the Si map more center-filled than the Ar map? The answer is unclear because Si and Ar are both expected at similar depths in the nucleosynthetic layer (e.g. Woosley, Heger & Weaver 2002). The relatively faint infrared emission of Si and S at the reverse shock may imply relatively less Si and S in the reverse shock. We suspect it is because the Si and S have condensed to solid form such as Mg protosilicate, $MgSiO_3$, Mg_2SiO_4 and FeS. In contrast, Ar remains always in the gas and does not condense to dust, so it should be infrared or X-ray emitting gas. Alternate explanation is that the ionization in the interior is due to photoionization from the X-ray shell (see Hamilton & Fesen 1988); in this case, the lack of interior Ar II relative to Si II might be due to its much higher ionization potential (16 eV compared to 8 eV). Theoretical models of nucleosynthesis, accounting for heating, photoionization, and column density of each element would be helpful for understanding the distribution of nucleosynthetic elements.

The Si and S emission detected at the interior, is most likely unshocked ejecta where the revere shock has not yet overtaken the ejecta. The radial profile of unshocked ejecta is centrally peaked at the time of explosion, as shown by Chevalier & Soker (1989). The radial profile of unshocked Fe ejecta is also expected to be center-filled for $\sim$1000 yr old Type Ia SNR of SN 1006 (Hamilton & Fesen 1988). The morphology of the featureless dust resembles that of unshocked ejecta, supporting the conclusion that the featureless dust is also freshly formed dust. The spectrum in Figure 1 (curve "d"), shows the resolved two lines at 26 μm and at 35 μm. The two respective lines at $\sim$26 μm may be resolved lines of [O IV] and [Fe II], and at $\sim$35 μm [Si II] and [Fe II] (as expected that the unshocked ejecta near the explosion center have a low velocity); alternatively, they could be highly doppler-shifted lines (in this case the two lines at 26 μm are both [O IV], and the two lines at 35 μm are both [Si II]). The newly revealed unshocked ejecta deserves extensive studies; preliminary doppler-shifted maps were presented in DeLaney et al. (2006) and the detailed analysis of velocities and abundances of unshocked and shocked ejecta will be presented in future papers (DeLaney et al. 2007; Smith et al. 2007).

3.   Spectral Fitting and Dust Composition

We performed spectral fitting to the IRS continua using our example regions in Figure 1. Included in the fitting are MIPS 24 μm and 70 μm fluxes (Hines et al. 2004), and the contribution of synchrotron emission (Figs. 3 and 5), estimated from the radio fluxes (DeLaney 2004) and Infrared Array Camera (IRAC) 3.6 μm fluxes (Ennis et al. 2006). We measured synchrotron radiation components for each position using radio maps and assuming the spectral index α=-0.71 (Rho et al. 2003) where log S $\propto \alpha$ log ν. Because the full-width-half-maximum of 24 μm is smaller than the IRS extracted region, the surface brightnesses for 24 μm were measured using a 15″ box, the same size as the area used for the extracted IRS LL spectra. We also made color corrections to each MIPS 24 μm data point based on each IRS spectrum and band-filter shape; the correction was as high as 25% for some positions. While the uncertainty of calibration errors in IRAC is 3-4%, that of MIPS 24 μm is better than 10%. The MIPS 70 μm image (Hines et al. 2004), shown in Figure 2e, clearly resolves Cas A from background emission, unlike the 160 μm image (Krause et al. 2005). Most of the bright 70 μm emission appears at the bright ring and corresponds to the 21 μm dust map and the shocked ejecta, particularly [Ar II], indicating that the 70 μm emission is primarily from freshly formed dust in the ejecta. The 70 μm emission also appears at the interior as shown in Figure 2e. We measured the brightness for 70 μm within a circle of radius 20″ for each position, accounting for the point-spread function (note that when the emission is uniform, the aperture size does not affect the surface brightness). We estimated the uncertainties of

the 70 μm fluxes to be as large as 30%. The largest uncertainty comes from background variation due to cirrus structures based on our selection of two background areas, 5′ to the northwest and south of the Cas A.

The dust continuum is fit with the Planck function ($B_\nu(T)$) multiplied by the absorption efficiency (Q_{abs}) for various dust compositions, varying the amplitude and temperature of each component. To determine the dust composition, we consider not only the grain species predicted by the model of dust formation in SNe (TF, N03), but also Mg protosilicates (ADM) and FeO (Henning et al. 1995) as possible contributors to the 21 μm feature. The optical constants of the grain species used in the calculation are the same as those of Hirashita et al. (2005), except for amorphous Si (Piller 1985), amorphous SiO_2 (Philipp 1985), amorphous Al_2O_3 (Begemann 1997), FeO (Henning et al. 1995), and we apply Mie theory (Bohren & Huffman 1983) to calculate the absorption efficiencies, Q_{abs}, assuming the grains are spheres of radii $a = 0.01$ μm. We fit both amorphous and crystalline grains for each composition, but it turned out that the fit results in Cas A (see §3) favor amorphous over crystalline grains. Thus, default grain composition indicates amorphous, hereafter. For Mg protosilicate, the absorption coefficients are evaluated from the mass absorption coefficients tabulated in Dorschner et al. (1980), and we assume that the absorption coefficient varies as λ^{-2} for $\lambda > 40$ μm, typical for silicates. We fit the flux density for each spectral type using scale factors C_i for each grain type i, such that $F_\nu^i = \Sigma_i\, C_i\, B_\nu\, Q_{abs,i}/a$. Note that the calculated values of Q_{abs}/a are independent of the grain size as long as $2\pi|m|a/\lambda <<1$ where m is the complex refractive index. Thus the derived scale factor C_i as well as the estimated dust mass (see §4) are independent of the radius of the dust. The dust compositions of the best fits are summarized in Table 1.

The strong 21 μm-peak dust is best fit by Mg proto-silicate, amorphous SiO_2 and FeO grains (with temperatures of 60-120 K) as shown in Figure 3. These provide a good match to the 21 μm feature. ADM suggested that the 21 μm feature is best fit by Mg proto-silicate while D01 suggested it is best fit by SiO_2 instead. We found, however, that SiO_2 produced a 21 μm feature that was too sharp. We also fit the observations using Mg_2SiO_4, which exhibits a feature around 20 μm and the overall variation of absorption coefficients of Mg_2SiO_4 with wavelength might be similar to that of Mg protosilicate (Dorschner et al. 1980; Jäger et al. 2003). However, with Mg_2SiO_4, the fit is not as good as that of Mg protosilicate, not only at the 21-μm peak, but also at shorter (10-20 μm) and longer (70 μm) wavelengths. Thus, we use Mg protosilicate and SiO_2 as silicates to fit the 21 μm-peak dust feature. The fit with Mg protosilicate, SiO_2 and FeO is improved by adding aluminum oxide (Al_2O_3, 83 K) and FeS (150 K), where Al_2O_3 improved the overall continuum shape between 10-70 μm and FeS improved the continuum between 30-40 μm (underneath the lines of Si, S and Fe), as shown Figure 3. The silicate composition is responsible for the 21 μm peak, suggesting

that the dust forms around the inner-oxygen and S-Si layers and is consistent with Ar being one of the oxygen burning products. We also include amorphous $MgSiO_3$ (480 K) and SiO_2 (300 K) to account for the emission feature around the 9.8 μm. The composition of the low temperature (40-90 K) dust component necessary for reproducing 70 μm is rather unclear. Either Al_2O_3 (80 K) (Model A in Table 1) or Fe (100 K) (Model B in Table 1 and Figure 4) can fit equally well, as listed in Table 1. We could use carbon instead of Al_2O_3 or Fe, but the line and dust compositions suggest the emission is from inner O, S-Si layers, where carbon dust is not expected. There are still residuals in the fit from the feature peaking at 21 μm (20-23 μm), and an unknown dust feature at 11-12.5 μm (it is not a part of typical PAH feature), as shown in Figure 3. The former may be due to non-spherical grains or different sizes of grains.

The weak 21 μm continuum is fit by FeO and Mg_2SiO_4 or Mg protosilicate (Models C and D in Table 1) since the curvature of the continuum changes at 20-21 μm as shown in Figure 5. To fit the rest of the spectrum, we use glassy carbon dust and Al_2O_3 grains. The glassy carbon grains (220 K) can account for the smooth curvature in the continuum between 8-14 μm. Carbon dust (80 K) and Al_2O_3 (100 K) contribute to the continuum between 15-25 μm. We could use Fe dust instead, but we suspect carbon dust because of the presence of relatively strong Ne line emission with the weak 21 μm dust class. Ne, Mg, and Al are all carbon burning products. We cannot fit the spectrum replacing carbon by Al_2O_3 with a single or two temperatures because Q_{abs}/a of Al_2O_3 has a shallow bump around 27 μm, thus the fit requires three temperature components of Al_3O_2 or a combination of two temperature components of Al_3O_2 and a temperature component of carbon. The continuum between 33-40 μm (underneath the lines of Si, S and Fe) can be optimally fit by FeS grains.

The 70 μm image shown in Figure 2e shows interior emission similar to the unshocked ejecta but that may also be due to projected circumstellar dust at the forward shock. In order to fit the featureless spectrum out to 70 μm, we must first correct for possible projected circumstellar dust emission. The exterior forward shock emission is most evident in the northern and northwestern shell. Taking the typical brightness in the NW shell ($\sim$20 MJy sr^{-1}), and assuming the forward shock is a shell with 12% radial thickness, the projected brightness is less than 4-10% of the interior emission ($\sim$40 MJy sr^{-1} after background subtraction). We assume that the remaining wide-spread interior 70 μm emission is from relatively cold, unshocked ejecta. Using the "corrected" 70 μm flux, the featureless spectra are equally reproduced by three models (Models E, F, and G) in Table 1 and Figures 6 and 7. All fits include $MgSiO_3$, FeO and Si, and either aluminum oxide, Fe, or a combination of the two are required at long wavelength. Carbon dust can also produce featureless spectra at low temperature but we exclude this composition because of the lack of Ne (produced from carbon burning). Aluminum oxide and Fe dust are far more likely to be associated with the

unshocked ejecta because they result from O-burning and Si-burning, respectively and the unshocked ejecta exhibit Si, S, and O+Fe line emission. However, one of the key challenges in SN ejecta dust is to understand featureless dust such as Fe, C, and aluminum oxide, and to link it to the associated nucleosynthetic products.

4. Dust Mass

We estimated the amount of freshly formed dust in Cas A based on our dust model fit to each of the representative 21 μm-peak, weak-21 μm, and featureless spectra (Fig. 1). The dust mass of i-grain type is given by:

$$M_{dust,i} = \frac{F_\nu^i \, d^2}{B_\nu(T_{d,i}) \, \kappa_i} = \frac{F_\nu^i d^2}{B_\nu(T_{d,i})} \frac{4 \, \rho_i \, a}{3 \, Q_{abs,i}}$$

where F_ν^i is the flux from i-grain species, d is the distance, B_ν is the Planck function, ρ_i is the bulk density, and a is the dust particle size. By employing the scale factor C_i and the dust temperature $T_{d,i}$ derived from the spectral fit, the total dust mass is given by $M_{dust} = \sum_i \rho_i \Omega d^2 C_i/3$, where Ω is the solid angle of the source. The total mass of the 21 μm-peak dust is then determined by summing the flux of all the pixels in the 21 μm-peak dust region (red region in Fig. 2f) and assuming each pixel in this region has the same dust composition as the spectrum in Fig. 3. We took the same steps for the weak-21 μm dust and the featureless dust.

The estimated total masses for each type of dust using a distance of 3.4 kpc (Reed et al. 1995) are listed in Table 1. Using the least massive composition in Table 1 for each of the three dust classes yields a total mass of 0.020 M$_\odot$ (the sum of masses from Models A, D, and F). Using the most-massive composition for each of the three dust classes yields a total mass of 0.054 M$_\odot$ (the sum of masses from Models B, C, and E). The primary uncertainty in the total dust mass between 0.020 and 0.054 M$_\odot$ is due to the selection of the dust composition, in particular for the featureless dust.

We also extracted a global spectrum of Cas A , but excluding most of the exterior forward shock regions. The spectrum is well fit with the combination of our three types of dust (including all compositions from Models A-G), as shown in Figure 8. We used the dust composition of Models A-G as a guideline in fitting the global spectrum, because the dust features (which were noticeable in representative spectra) were smeared out. Our goal in fitting the global spectrum is to confirm consistency between the mass derived from global spectrum and that derived from representative spectra described above. The total estimated mass from the global spectrum fit is $\sim$0.028 M$_\odot$, being consistent to the mass

determined from the individual fits to each dust class. The respective dust mass for each grain composition is listed in Table 3. The masses of $MgSiO_3$, SiO_2, FeS and Si are more than a factor of ten to hundred smaller than the predictions; the predictions (N03 and TF) also have the dust features at 9 μm for $MgSiO_3$, 21 μm for SiO_2, and 30-40 μm for FeS stronger than the observed spectra if the dust mass is increased. The carbon mass is also a factor of 10 lower than the predictions. We were not able to fit the data with as much carbon dust mass as expected, even if we use the maximum carbon contribution allowed from the spectral fits.

5. Discussion

We find an estimated total freshly-formed dust mass of 0.020-0.054 $M_\odot$ is required to produce the mid-infrared continuum up to 70 μm. The dust mass we derive is orders of magnitude higher than the two previous infrared estimates of 3.5×10^{-3} $M_\odot$ and 7.7×10^{-5} $M_\odot$, which are derived by extrapolation from 1.6×10^{-4} $M_\odot$ (D01) and 2.8×10^{-6} $M_\odot$ (ADM) for selected knots, respectively. One of the primary reasons for our higher mass estimate is that we include fluxes up to 70 μm while the fits in D01 and ADM accounted for dust emission only up to 30 and $\sim$40 μm, respectively. The cold dust (40-150 K) has much more mass than the warmer (>150 K) dust. In addition, our IRS mapping over nearly the entire extent of Cas A with higher spatial and spectral resolutions provides more accurate measurements, while D01 and ADM covered only a portion of the remnant. In addition, ADM use only Mg protosilicate dust; the absorption coefficient for Mg protosilicate is a few times larger than those of other compositions.

Our dust mass estimate is also at least one order of magnitude higher than the estimate of 3×10^{-3} $M_\odot$ by Hines et al. (2004). They fitted MSX and *Spitzer* MIPS data with Mg protosilicate. Note that they used only one composition. They derived a freshly synthesized dust mass of 3×10^{-3} $M_\odot$ at a temperature of 79-82 K and a smaller dust mass of 5×10^{-6} $M_\odot$ at a higher temperature of 226-268 K, and they explained that the mass estimate depends on the chosen dust temperature. As ADM mentioned, the absorption coefficient for Mg protosilicate is a few times larger than those of other compositions. Therefore, even including the long-wavelength data, the estimated mass was small since only Mg protosilicate was modeled. With the photometry in Hines et al. (2004), one could easily fit the data with only Mg protosilicate and would not need additional grain compositions. However, with the accurate IRS data, many dust features and the detailed continnum shape could not be fit solely with the Mg protosilicate. Note that the continuum shapes of weak 21 μm dust and "featureless" dust are very different from the shape of protosilicate absorption coefficient.

Therefore, it was necessary to include many other compositions in order to reproduce the observed IRS spectra.

It should be noted here that, in contrast with the previous works, we introduced Si and Fe–bearing materials such as Si, Fe, FeS and FeO. We explain why we included such dust in our model fitting as follows. Firstly, we included Si and Fe dust because these elements are significant outputs of nucleosynthesis; indeed Woosley & Weaver (1995) show that Si and Fe are primary products in the innermost layers of the ejecta. Secondly, we observed strong Si and Fe lines in the infrared and X-ray spectra; strong Si lines were detected in the *Spitzer* spectra, as shown in Figure 1 (also see D01), and the Fe line detection at 17.9 μm is also shown in Figure 5. (The Fe maps at 17.9 μm and at 1.64 μm were presented in Ennis et al. (2006) and Rho et al. (2003), respectively.) Si and Fe lines from ejecta are also bright in X-ray emission (Hwang, Holt & Petre 2000). Thirdly, dust such as Si, Fe, FeO and FeS is predicted to form in the ejecta of Population III supernovae (N03). TF and N03 predict Fe_3O_4 instead of FeO in the uniformly mixed ejecta where the elemental composition is oxygen-rich, but the kind of iron-bearing grains in oxygen-rich layers of the ejecta is still uncertain, partly because the surface energy of iron is very sensitive to the concentration of impurities such as O and S (as was discussed by Kozasa & Hasegawa (1988)), and partly because the chemical reactions at the condensation of Fe-bearing dust is not well understood. Depending on the elemental composition and the physical conditions in the ejecta, it is possible that Fe, FeO and/or FeS form in the oxygen-rich layers of Galactic SNe. The observations of Cas A favor FeO dust over Fe_3O_4, in order to match the spectral shape of the 21 μm-peak dust and the weak-21 μm dust. This aspect should be explored theoretically in comparison with the observations in the future.

Our total mass estimate is also about one order of magnitude higher than the estimate of 6.9×10^{-3} M$_\odot$ by Dwek (1987), who used IRAS fluxes (possibly confused by background cirrus) and assumed a silicate–type dust as stellar or supernova condensates being present in supernova cavity and heated up by the reverse shock. Our estimated mass is much less than 1 M$_\odot$, which Wilson & Batrla (2005) suggested may still be associated with the ejecta, after accounting for results of high-resolution CO observations. Our estimated mass of 0.020 to 0.054 M$_\odot$ is only derived for wavelengths up to 70 μm, so it is still possible that the total freshly-formed dust mass in Cas A is higher than our estimate because there may be colder dust present. Future longer-wavelength observations with Herschel, SCUBA-2 and ALMA are required to determine if this is the case. Also note that we did not include any mass from fast moving knots projected into the same positions as the forward shock, such as in the northeast and southwest jets, and the eastern portions of the SNR outside the 21 μm-peak dust region (see Fig. 2e), because such dust could not be cleanly separated from the interstellar/circumstellar dust.

We can use our dust mass estimate in conjunction with the models of N03 and TF to understand the dust observed in the early universe. If the progenitor of Cas A was 15 $M_\odot$, our estimated dust mass (0.020-0.054 $M_\odot$) is 7–18% of the 0.3 $M_\odot$ predicted by the models. If the progenitor mass was 30 $M_\odot$, then the dust mass is 2–5% of the 1.1 $M_\odot$ predicted by the models. One reason our dust mass is lower than predicted by the models is that we cannot evaluate the mass of very cold dust residing in the remnant from the observed spectra up to 70 μm as described above, unless the predicted mass is overestimated. Another reason is that when and how much dust in the remnant is swept up by the reverse shock is highly dependent on the thickness of the hydrogen envelope at the time of explosion and that the evolution and destruction of dust grains formed in SNe strongly depend not only on their initial sizes but also the density of ambient interstellar medium (Nozawa et al. 2007). Dust formation occurs within a few hundred days after the SN explosion (Kozasa et al. 1989; TF; N03). Without a thick hydrogen envelope, given an age for Cas A of $\sim$300 years, a significant component of dust may have already been destroyed if dust grains formed in the ejecta were populated by very small-sized grains; otherwise, it is possible that some grain types may be larger, which would increase the inferred mass.

We observed most of the dust compositions predicted by SN Type II models, and the global ejecta composition is consistent with the unmixed-case N03 model than mixed-case model; however, note that different morphologies of Ar and Si maps imply that some degree of mixing has occurred. Our estimated dust mass with *Spitzer* data is one order of magnitude smaller than the predicted models of dust formation in SNe ejecta by N03 and TF, but one to two orders of magnitude higher than the previous estimations. We now compare the dust mass in high-redshift galaxies with the observed dust mass of Cas A based on the chemical evolution model of Morgan & Edmunds (2001). By a redshift of 4, SNe have been injecting dust in galaxies for over 2 billion years and there is enough dust from SNe to explain the lower limit on the dust masses ($\sim$7$\times$10^7 $M_\odot$) inferred in submm galaxies and distant quasars (Chini & Kruegel 1994; Isaak et al. 2002). It should be noted with the dust mass per SN implied by our results for Cas A alone, the interpretation of dust injection from SNe is limited, because the amount of dust built up over time is strongly dependent on the initial mass function, stellar evolution models and star formation rates (Morgan & Edmunds 2003), and destruction rates in supernova are believed to be important at timescales greater than a few billion years. Additional infrared/submm observations of other young supernova remnants and supernovae are crucial to measure physical processes of dust formation in SNe including the dust size distribution, composition and dependence on nucleosynthetic products and environment, and to understand the dust in the early Universe in terms of dust injection from SNe.

6.   Conclusion

1. We presented *Spitzer* IRS mapping covering nearly the entire extent of Cas A and examined if SNe are primary dust formation sites that can be used to explain the high quantity of dust observed in the early Universe.

2. The ejecta maps, show a remarkable similarity to the dust maps, thereby confirming that dust formation occurs in the SN ejecta.

3. The IRS spectra of Cas A show a few dust features such as an unique 21 μm peak in the continuum from Mg protosilicate, SiO_2, and FeO. We observed most of the dust compositions predicted by SN Type II dust models. However, the dust features in Cas A favour Mg protosilicate rather than Mg_2SiO_4, and FeO rather than Fe_3O_4. The composition infers that the ejecta are unmixed.

4. Our total estimated dust mass with *Spitzer* observations ranging from 5.5 - 70 μm is 0.020-0.054 M$_\odot$, one order of magnitude smaller than the predicted models of dust formation in SNe ejecta by N03 and TF, but one or more orders of magnitude higher than the previous estimations. The freshly formed dust mass derived from Cas A is sufficient from SNe to explain the lower limit on the dust masses in high redshift galaxies.

REFERENCES

Arendt, R. G., Dwek, E., & Moseley, S. H. 1999, ApJ, 521, 234 (ADM)

Begemann, B. et al., 1997, ApJ, 476, 1991

Bertoldi, F., Carilli, C. L., Cox, P., Fan, X., Strauss, M. A., Beelen, A., Omont, A., Zylka, R., 2003, å,406, 55

Bohren, C. F., Huffman, D. R., 1983, Absorption and scattering of light by small particles, New York

Chevalier, R. & Soker1989, ApJ, 341, 867

Chini, R. & Kruegel, E., 1994, A&A, 288, L33

Clayton, D.D., Deneault, E. A.-N., Meyer, B.S., 2001, ApJ, 562, 480

DeLaney T., 2004, PhD thesis, U. Of Minnesota

DeLaney, T., Smith, J., Rudnick, L., Ennis, J., Rho, J., Reach, W., Kozasa, T., Gomez, H., 2006, BAAS, 208, 59.03

DeLaney, T., Smith, J., Rudnick, L., Ennis, J., Rho, J., Reach, W., Kozasa, T., Gomez, H., 2007, in preparation

Dorschner, J., Friedmann, C., Gütler, J., & Duley, W. W. 1980, Ap&SS, 68 159

Douvion, T., Lagage, P. O. & Pantin, E. 2001, A&A, 369, 589 (D01)

Dunne, L., Eales, S., Ivison, R., Morgan, H., & Edmunds, M. 2003, Nature, 424, 285

Dwek, E., Hauser, M. G., Dinerstein, H. L., Gillett, F. C., Rice, W. 1987, ApJ, 315, 571

Dwek, E. 2004, ApJ, 607, 848

Dwek, E., Galliano, F. & Jones, A. P. 2007, ApJ 662, 927

Ennis, J. et al., 2006, ApJ, 652, 376

Ercolano, B., Barlow, M. J., & Sugerman B. E. K., 2007, MNRAS, 375, 753

Fesen, R. A. 2001, ApJS, 133, 161

Gotthelf, E. V. et al., 2001, ApJL, 552, 39

Gomez H., Dunne L., Eales S., Gomez E., Edmunds M., 2005, MNRAS, 361, 1012

Gao, Y., Carilli, C.L., Solomon, P.M., Vanden Bout, P.A., 2007, ApJ, 660, L93

Hamilton, A. J. & Fesen, R. 1988, ApJ, 327, 178.

Henning, Th., Begemann, B., Mutschke, H., Dorschner, J, 1995, A&A Suppl. Ser. 112, 143

Hines, D. C. et al. 2004, ApJS, 154, 333

Hirashita, H., et al., 2005, MNRAS 357, 1077

Hwang, U., Holt, S. S., & Petre, R. 2000, 537, L119

Hwang, U., et al., 2004, ApJ, 615, 117

Isaak, K. G., Priddey, R. S., McMahon, R. G., Omont, A. et al. 2002, MNRAS, 329, 149

Jäger, C., Dorschner, J., Mutschke, H., Posch, Th., Henning, Th. 2003, A&A, 408, 193

Kennicutt, R.C., Jr. et al., 2003, PASP, 115, 928

KifonidisK., Plewa, T., Janka, H.-T., & Müller, E. 2000, ApJ, 531, L123

Kozasa, T., & Hasegawa, H. 1988, Icarus, 73, 180

Kozasa, T., Hasegawa, H. & Nomoto, K. 1989, ApJ, 334, 325

Kozasa, T., Hasegawa, H., & Nomoto, K. 1991, A&A, 249, 474

Krause, O., et al., 2004, Nature, 432, 596

Lagage, P. O. et al., 1996, A&A, 315, L273

Maiolino et al. 2006, Memorie della Societa Astronomica Italiana, 77, 643

McCray, R. 1993, ARA&A, 31, 175

Meikle, W. P. S. et al. 2007, ApJ, 665,

Morgan, H. L., Dunne, L., Eales, S. A., Ivison, R. J., & Edmunds, M. G. 2003, ApJ, 597, L33

Morgan, H. L. & Edmunds, M. G. 2003, MNRAS, 343, 427

Nozawa, T., Kozasa, T., Umeda, H., Maeda, K., & Nomoto, K. 2003, ApJ, 598, 785 (N03)

Nozawa, T. et al. 2007, ApJ preprint, arXiv:0706.0383

Pei, Y. C. & Fall, S. M., 1995, ApJ, 454, 69

Pérez-Rendón B., García-Segura, G., & Langer, N., 2002, Ionized Gaseous Nebulae, Eds. W. J. Henney, J. Franco, M. Martos, & M. Pëna, Revista Mexicana de Astronomía y Astrofíca, 12, 94

Philipp, H. 1985, *Handbook of Optical Constamts of Solids*, ed. E. D. Palik, Academic Press, San Diego,749

Piller, H. 1985, *Handbook of Optical Constamts of Solids*, ed. E. D. Palik, Academic Press, 571

Reed, J.E., Hester, J.J., Fabian, A.C., & Winkler, P.F., 1995, ApJ, 440, 706

Rho, J., Reynolds, S.P., Reach, W.T., Jarrett, T.H., Allen, G.E., & Wilson, J.C. 2003, ApJ, 592, 299

Smail I., Ivison R.J., Blain A.W., 1997, ApJ, 490, L5

Smith, J. D. T., Armus, L., Dale, D.A., Roussel, H., Sheth, K., Buckalew, B.A., Jarrett, T. H., Helou, G., & Kennicutt, R. C., 2007, PASJ, submitted

Sugerman, Ben E. K. et al., 2006, Science, 313, 196

Todini, P. & Ferrara, A., 2001, MNRAS, 325, 726 (TF)

van den Bergh, S., 1971, ApJ, 165, 457

Wilson T.L., & Batrla W., 2005, A & A, 430, 561

Woosley, S. E., & Weaver, T. A., 1995, ApJS, 101, 181

Woosley, S. E., A. Heger, & Weaver, T. A 2002, Reviews of Modern Physics, 74, 1015

Young, P. A. et al. 2006, ApJ, 640, 891

Whittet D.C.B., 2003, Dust in the Galactic Environment, Second Edition, IOP, Cambridge University Press, UK

Table 1.   Properties of Freshly Formed Dust in Cas A

Dust Type (spectrum in Fig. 1)	Model	Compositions[a]	Strong Lines	Nucleosynthesis Layers	Mass ($M_\odot$)
21μm-peak (a)	A	**Mg protosilicate**, **MgSiO$_3$**, SiO$_2$, FeO, FeS, Si, *Al$_2$O$_3$*	Ar	Inner-O, S-Si	0.0030
21μm-peak	B	**Mg protosilicate**, **MgSiO$_3$**, FeO, SiO$_2$, FeO, FeS, Si, *Fe*	Ar	Inner-O, S-Si	0.0120
weak-21μm (b)	C	**C-glass**, **FeO**, Al$_2$O$_3$, Si, *Mg$_2$SiO$_4$*	Ne, Si, Ar (S, O+Fe)	C-burning	0.0180
weak-21μm	D	**C-glass**, **FeO**, Al$_2$O$_3$, Si, FeS, *Mg protosilicate*	Ne, Si, Ar (S, O+Fe)	C-burning	0.0157
Featureless (d)	E	**MgSiO$_3$**, **Si**, FeS, *Fe, Mg$_2$SiO$_4$*	Si, S, (O+Fe)	O, Al burning (Fe-Si-S)	0.0245
Featureless	F	**MgSiO$_3$**, **Si**, FeS, *Fe, Al$_2$O$_3$*	Si, S, (O+Fe)	O, Al burning (Fe-Si-S)	0.0171
Featureless	G	**MgSiO$_3$**, **Si**, FeS, *Al$_2$O$_3$, Mg$_2$SiO$_4$*	Si, S, (O+Fe)	O, Al burning (Fe-Si-S)	0.0009

[a]Compositions in the best fit, where a few primary compositions are written in bold, and alternative dust compositions are in italics.

Table 2.   Mass of dust with each composition

Composition	Model A[a]	Model B	Model C	Model D	Model E	Model F	Model G
Al_2O_3	6.66E-05 (083)	0.00E+00 (000)	5.13E-05 (105)	1.03E-04 (100)	0.00E+00 (000)	8.13E-04 (050)	6.50E-04 (060)
C glass	0.00E+00 (000)	0.00E+00 (000)	2.08E-03 (80/180)	1.07E-03 (80/220)	0.00E+00 (000)	0.00E+00 (000)	0.00E+00 (000)
$MgSiO_3$	1.19E-08 (480)	1.19E-08 (480)	0.00E+00 (000)	0.00E+00 (000)	2.55E-05 (110)	3.19E-05 (110)	2.55E-05 (110)
Mg_2SiO_4	0.00E+00 (000)	0.00E+00 (000)	7.89E-05 (120)	0.00E+00 (000)	1.72E-06 (130)	0.00E+00 (000)	3.00E-06 (130)
Mg protosilicate	5.00E-05 (120)	4.67E-05 (120)	0.00E+00 (000)	3.77E-05 (120)	0.00E+00 (000)	0.00E+00 (000)	0.00E+00 (000)
SiO_2	2.23E-03 (060/300)	1.40E-03 (065/300)	0.00E+00 (000)	0.00E+00 (000)	0.00E+00 (000)	0.00E+00 (000)	0.00E+00 (000)
Si	4.34E-04 (096)	4.34E-04 (100)	1.63E-03 (090)	8.17E-03 (080)	9.32E-04 (090)	1.24E-04 (120)	6.21E-05 (120)
Fe	0.00E+00 (075)	9.82E-03 (110)	0.00E+00 (000)	0.00E+00 (000)	2.16E-02 (95/135)	1.36E-02 (100/150)	0.00E+00 (000)
FeO	1.13E-04 (105)	2.11E-04 (095)	1.39E-02 (060)	5.97E-03 (065)	0.00E+00 (000)	0.00E+00 (000)	0.00E+00 (000)
FeS	1.20E-04 (150)	2.11E-04 (150)	0.00E+00 (000)	3.40E-04 (120)	1.94E-03 (055)	2.59E-03 (055)	1.29E-04 (100)

[a]The numbers in parentheses are dust temperatures, and two numbers indicate two temperatures.

Table 3. Mass of dust with each composition

Composition	Predicted ($M_\odot$)	Model (A+D+G)[a]	Model (B+C+E)[b]	Mass (global)[c]
Al_2O_3	2.40E-04 $\sim$ 9.00E-03	8.20E-04	5.1300E-05	1.22E-04 (105)
carbon	7.00E-02 $\sim$ 3.00E-01	1.07E-03	2.0767E-03	2.04E-03 (070/265)
$MgSiO_3$	2.00E-03 $\sim$ 7.00E-3	2.55E-05	2.5500E-05	1.65E-04 (110)
Mg_2SiO_4	3.70E-02 $\sim$ 4.40E-1	3.00E-06	8.0620E-05	3.21E-05 (120)
Mg protosilicate	[d] none	8.77E-05	4.6710E-05	6.70E-05 (110)
SiO_2	2.50E-02 $\sim$ 1.400E-01	2.23E-03	1.3964E-03	1.35E-03 (065)
Si	7.00E-02 $\sim$ 3.00E-01	8.66E-03	2.9989E-03	4.42E-03 (080)
Fe	2.00E-02 $\sim$ 4.00E-02	0.00E+00	3.1459E-02	1.03E-02 (090)
FeO	[d] none	6.08E-03	1.4136E-02	6.23E-03 (070)
FeS	4.00E-02 $\sim$ 1.10E-01	5.90E-04	2.1501E-03	2.90E-03 (090)

[a]The sum of the masses using the least massive composition among models.

[b]The sum of the masses using the most-massive compositions.

[c]The mass using the global spectrum.

[d]see the text for details.
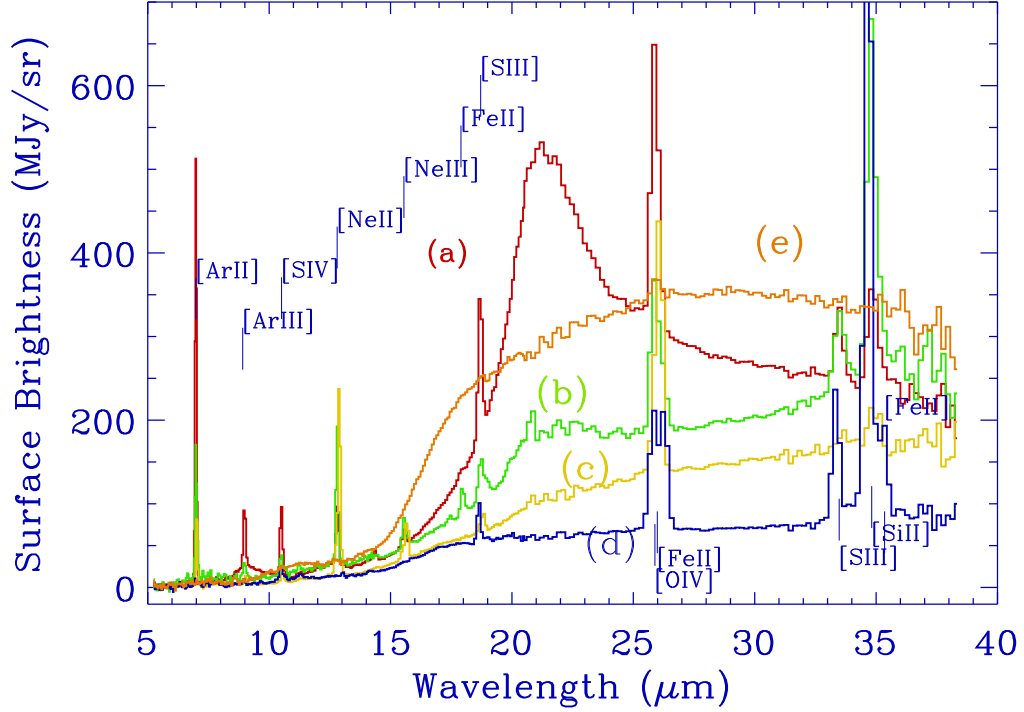
Fig. 1.— Representative Set of *Spitzer* IRS spectra of Cas A. The contrast between continuum shape and line emission is noticeable. Many of the strong ejecta lines are seen including [Ar II] (7 μm), [Ar III] (8.9 μm), [Si IV] (10.5 μm), [Ne II] (12.8 μm), [Ne III] (15.5 μm), [S III](18.7 μm), [O IV] and [Fe II] (26 μm), [S III] (33.5 μm), [Si II] (34.8 μm), and [Fe II] (35.3 μm). The dominant continuum shapes are 21 μm-peak dust showing a dust feature at 21 μm often accompanied by a silicate emission feature at 9.8 μm with strong Ar lines (red, curve a) and weak-21 μm dust with relatively strong Ne lines compared with Ar (green curve, b). Featureless spectra include the continuous rising spectra (yellow, c), and the gently rising spectra (blue, d) with strong O+Fe or Si lines. The positions of RA. and Dec. are 350.900, 58.8356 (a), 350.812, 58.8075 (b), and 350.879 58.7911 (c), 350.857, 58.815 (d), and 350.862 58.8550 9 (e). For illustration, the spectra were multiplied by 1.4 (curve a), 2.8 (b), 0.8 (c), 1.5 (d), and 2 (e), respectively. "Broad" continuum spectra arise from interstellar/circumstellar medium (orange, e).

Fig. 2.— (a) 21 μm dust map; a continuum map of 19-23 μm subtracted by the baselines of neighboring wavelengths. This dust map is remarkably similar to the [Ar II] map (b) the resolutions are convolved to match to each other). The image is centered at R.A. $23^h23^m25.86^s$ and Dec. $+58°49'14''$ (J2000), and covers an $7.87'$ by $5'$ field of view. (c) A combination of [O IV] and [Fe II] line map at 26 μm. (d) [Si II] (34.8 μm) map. (e) MIPS 70 μm map from Hines et al. (2004). The locations of the forward and reverse shock boundaries are marked as ellipses where we adjusted for elongation from Gotthelf et al. (2001) using long-exposure *Chandra* archival data (Hwang et al. 2004). (f) Distributions of three major groups of dust types : 21μm-peak dust regions are in red (spectrum (a)), weak-21μm dust regions are in green (spectrum (b)), and featureless-dust regions are in blue ((d) spectrum in Fig. 1). *(Fig. 2 is a jpeg file)*
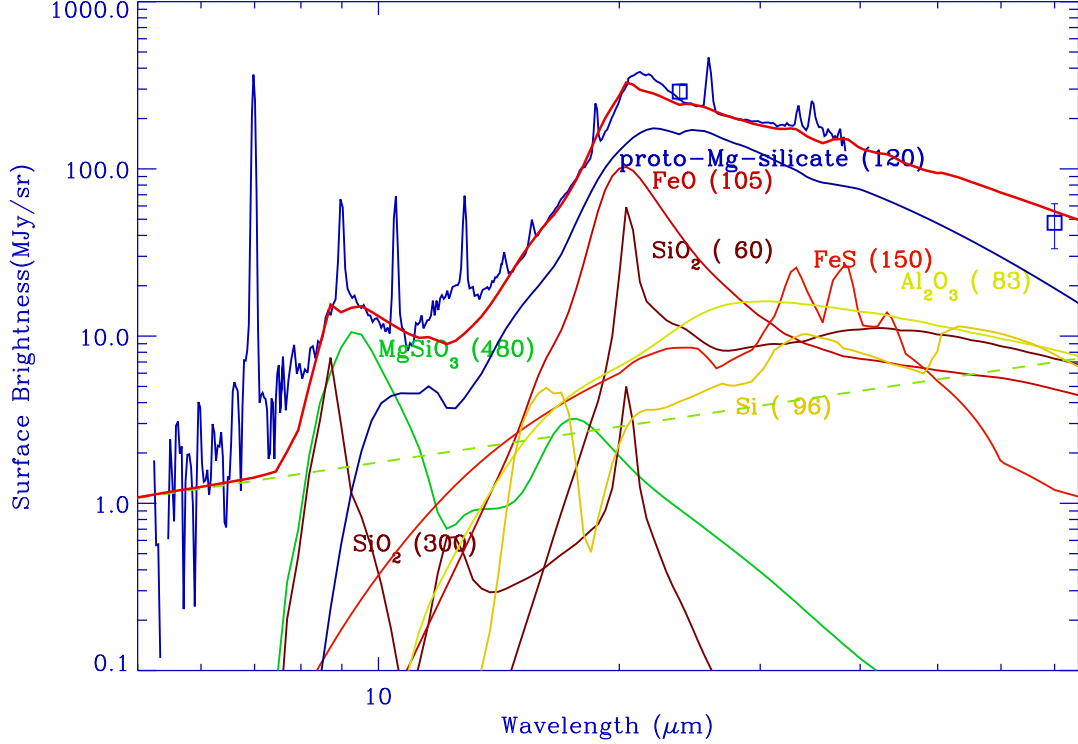
Fig. 3.— 21 μm-peak dust spectrum superposed on the dust fit of Model A: A *Spitzer* IRS spectrum towards a bright part of the northern shell fitted with dust compositions of Mg proto-silicate, $MgSiO_3$, SiO_2, FeO, and Al_2O_3. The compositions suggest that the dust forms around inner-oxygen and S-Si layers. The data and the total fit are shown in blue and thick red lines, respectively, and MIPS fluxes are marked with squares. The dust temperatures are shown in parentheses, and the dotted lines are from the second temperature components. Synchrotron continuum contribution (green dashed line) is estimated based on the radio fluxes and IRAC 3.6μm image.
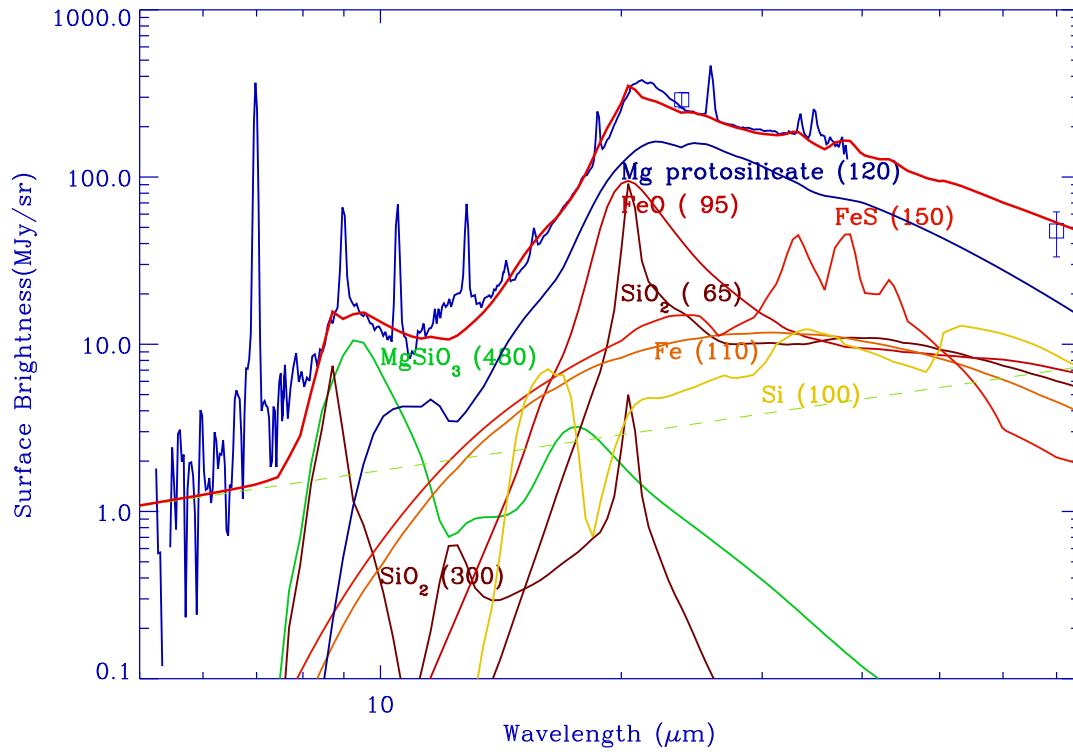
Fig. 4.— 21 μm-peak dust superposed on the dust fit of Model B.
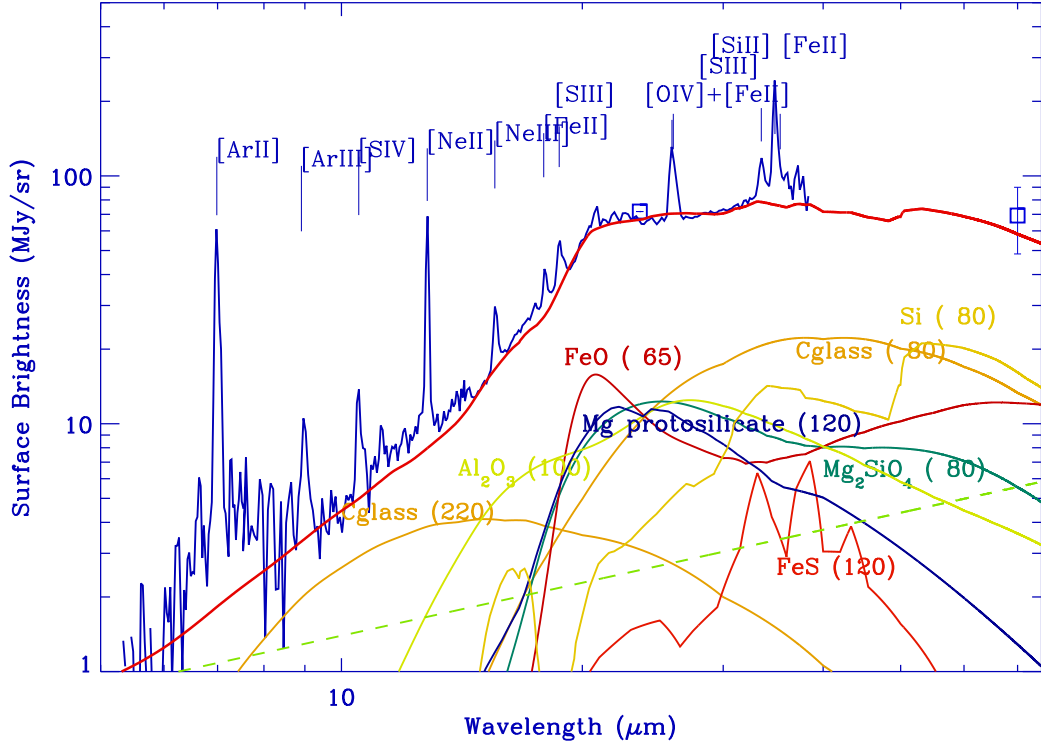
Fig. 5.— Weak-21 μm dust superposed on the dust fit of Model D: A second type of dust continuum in Cas A. The distribution of this type of dust is shown in Fig. 2f, in green.
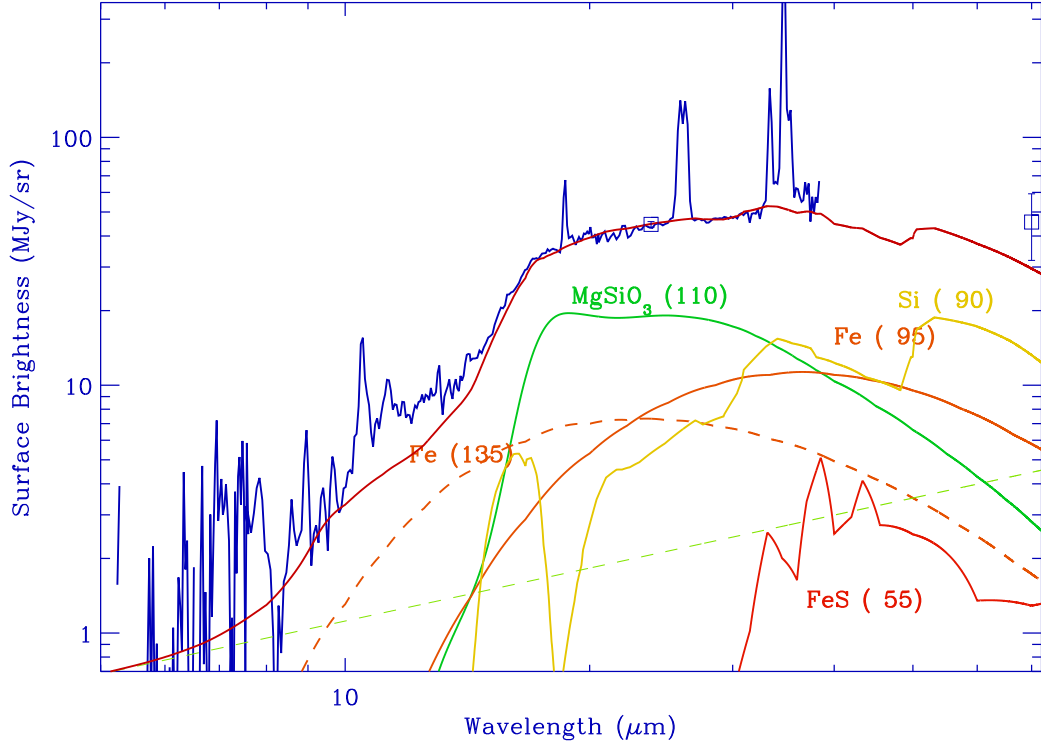
Fig. 6.— Featureless Dust Spectrum: the continuum can be fit with MgSiO$_3$ and Fe (Model E). The featureless spectra accompanies with S, Si, and O/Fe lines. The green dashed line is predicted synchrotron emission model.
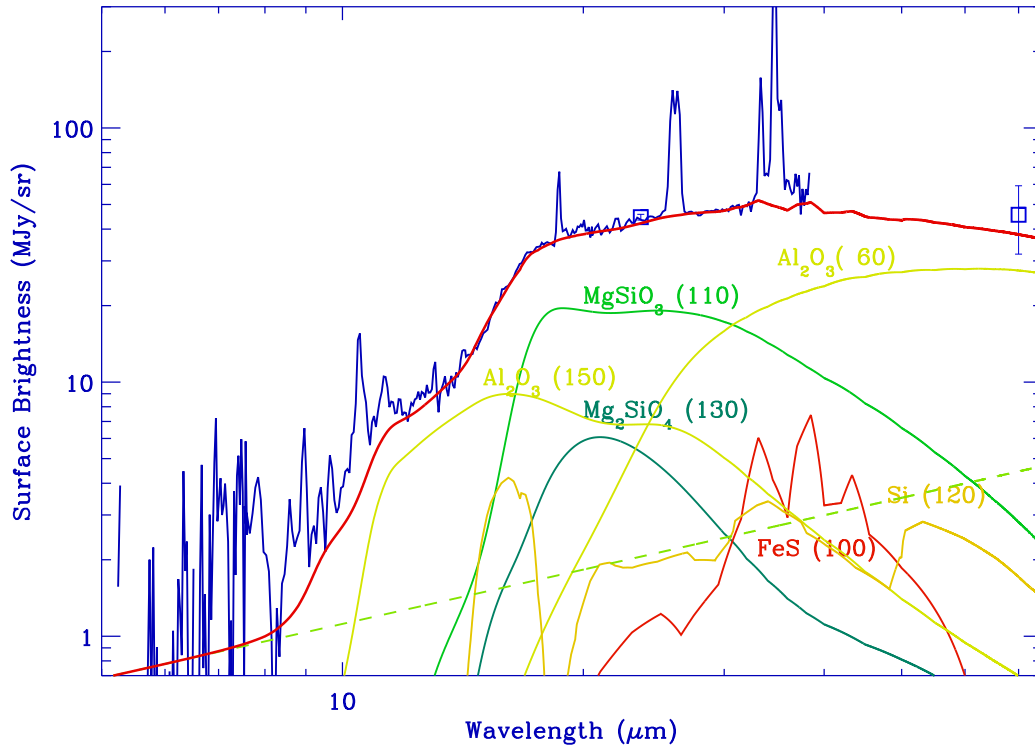
Fig. 7.— Featureless Dust Spectrum: The continuum can be fit with Al_2O_3, and $MgSiO_3$ (Model G).
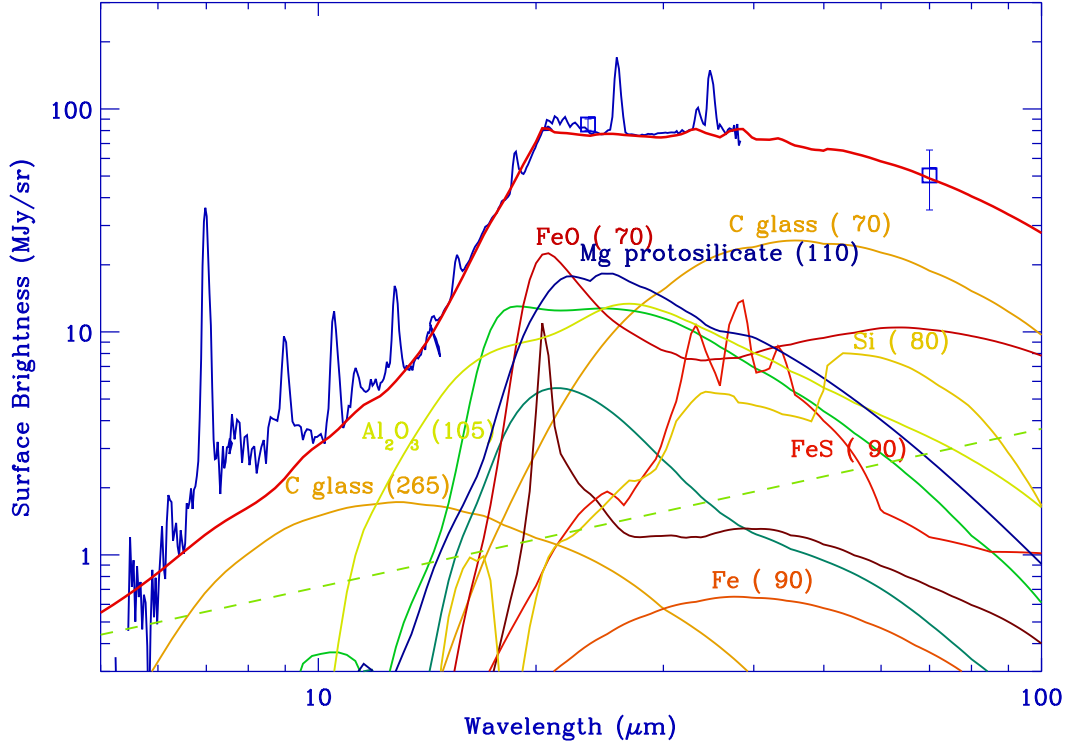
Fig. 8.— Total spectrum of Cas A and the dust fit of grains with a few primary contributions of grain models. The dark green and brown lines are MgSiO$_3$ (100 K) and SiO$_2$ (65K), respectively. The green dashed line is predicted synchrotron emission model.

This figure "f2.jpg" is available in "jpg" format from:

http://arXiv.org/ps/0709.2880v1